Observation of Hydrodynamic Flows in Imploding Fusion Plasmas on the National Ignition Facility

Observations of hydrodynamic flows in imploding fusion plasmas on the NIF

D.J. Schlossberg[1], G.P. Grim[1], D.T. Casey[1], A.S. Moore[1], R. Nora[1], B. Bachmann[1], L.R. Benedetti[1], R.M. Bionta[1], M.J. Eckart[1], J.E. Field[1], D.N. Fittinghoff[1], M. Gatu Johnson[2], V. Geppert-Kleinrath[3], E.P. Hartouni[1], R. Hatarik[1], W.W. Hsing[1], L.C. Jarrott[1], S.F. Khan[1], J.D. Kilkenny[4], O.L. Landen[1], B.J. MacGowan[1], A.J. Mackinnon[1], K.D. Meaney[3], D.H. Munro[1], S.R. Nagel[1], A. Pak[1], P.K. Patel[1], B.K. Spears[1], P.L. Volegov[3], C.V. Young[1]

[1]*Lawrence Livermore National Laboratory, Livermore, California 94550, USA*
[2]*Massachusetts Institute of Technology Plasma Science and Fusion Center, Cambridge, Massachusetts 02139, USA*
[3]*Los Alamos National Laboratory, Los Alamos, New Mexico 87544, USA*
[4]*General Atomics, La Jolla, California 92121, USA*

Inertial confinement fusion implosions designed to have minimal fluid motion at peak compression often show significant linear flows in the laboratory, attributable per simulations to percent-level imbalances in the laser drive illumination symmetry. We present experimental results which intentionally varied the Mode 1 drive imbalance by up to 4% to test hydrodynamic predictions of flows and the resultant imploded core asymmetries and performance, as measured by a combination of DT neutron spectroscopy and high-resolution x-ray core imaging. Neutron yields decrease by up to 50% and anisotropic neutron Doppler broadening increases by 20%, in agreement with simulations. Furthermore, a tracer jet from the capsule fill tube perturbation that is entrained by the hot spot flow confirms the average flow speeds deduced from neutron spectroscopy.

Inertial confinement fusion relies on balanced compression of a target to areal densities large enough to confine a burning, thermonuclear plasma [1]. During indirect-drive inertial confinement fusion (ICF), lasers focused on the inner walls of a high-Z cavity convert laser energy into thermal x-rays. These x-rays then impinge on a spherical target within the cavity, ablating its outer layer and driving the implosion. Uniformity in compression is critical for achieving high performance and coupling the maximum amount of energy into the implosion.

However, implosions are generally observed to have low-mode, volumetric asymmetries that are hypothesized to be due to laser drive asymmetry [2,3,4,5,6] and center-of-mass motion [7,8] of the fusing plasma ("hot spot"). These asymmetries degrade performance through several channels, including increased conduction losses [9], radiative losses [10,11], and residual kinetic energy left unconverted to thermal energy [12]. At the National Ignition Facility (NIF), recent implosions with the largest performance discrepancy between 2D predictions and experiment are seen to have large mode 1 asymmetries [13,14] in the shell areal density and hot spot velocity.

In this letter, we report results from systematically manipulating radiation-drive asymmetry to evaluate effects on implosion performance. To isolate effects from asymmetric drive, we kept the capsule, fuel, high-Z cavity, laser pulse shape and total power constant, and varied the balance of laser energy entering each end of the cavity. Larger laser imbalance produces stronger capsule-drive asymmetry. As this drive asymmetry increases, we find increased hot spot drift velocity (v_{HS}), degraded neutron yield, broadened neutron energy spectra, limb-brightening in x-ray images, and stronger vortical flow-fields internal to the fusing plasma. These degradations directly inform ignition-type implosions. Results agree with trends in recent theoretical work [15,16,17], which provides a framework for interpreting effects of fuel velocity-variance on observed neutron energy spectra. Two-dimensional, hydrodynamic simulations agree with trends, though discrepancies exist in absolute parameter values. The dominant flow within the hot spot is directly imaged through a tracer reaching > 200 km/s through deuterium-tritium (DT) plasmas of density > 10 g/cm^3 and pressures > 10 Gbar. These flows imply a significant fraction of radiation drive remains as residual kinetic energy. The measured, time-resolved fluid motion tracks predicted paths, and has comparable magnitudes to simulated values. This work presents a consistent understanding across experiment, simulation, and theory of the effect of low-mode drive asymmetries on ICF implosions.

Figure 1 depicts experimental details of this set of implosions. The target comprised a 5.4 mm dia. by 10.13 mm tall gold cavity ("hohlraum") [Fig. 1(a)], inside which was suspended a hollow capsule with a 64-µm thick high-
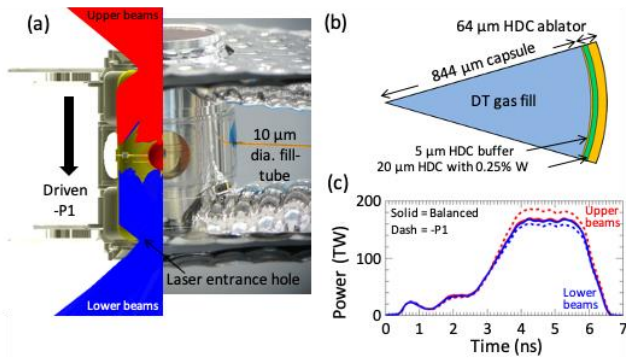
Figure 1: (a) Hohlraum model and photo, with example P1 drive; (b) SymCap constituents; (c) Example laser drive waveforms

Figure 2: nToF velocities along four lines-of-sight, overlaid on a neutron activation skymap; lines of latitude (longitude) are on 15° (30°) intervals and centered at 90° (270°). "FT" denotes the fill tube location, and the -P1/P0 case shown is shot N171022-001.

density carbon (HDC) ablator shell [Fig. 1(b)]. A 25-µm thick portion of this shell was doped with 0.25% tungsten, shown to improve performance [18,19]. Gaseous DT fuel was fed into the capsule before each implosion via a 10-µm diameter fill tube, shown in Figure 1(a). Using gaseous DT fuel with added mass-equivalent ablator as surrogates for an ignition-type DT-ice layer has successfully tuned symmetry of capsules [6, 20], with accurate scaling to ignition-relevant targets. Here, targets were cooled to 32 K to achieve the required hohlraum ^{4}He fill density (0.3 mg/cm^3) and DT fuel density (~4 mg/cm^3). The gold hohlraum walls were then illuminated with a 1.1 MJ, 340 TW peak-power laser pulse shown in Figure 1(c). The pulse shape matched the high performance, high-adiabat "Bigfoot" pulse [20,21]. Simulations show 94% of the HDC shell was ablated. Average energy was kept sufficiently constant from shot-to-shot, with total energy in the peak reproducible to ±0.8% across all cases. X-ray drive asymmetries were induced only by altering the balance of upper/lower NIF outer cone power during the peak drive, with a maximum of ±8%. An example asymmetric pulse is shown in Figure 1(c) as dashed lines and corresponds to the driven $-P1$ direction shown in (a).

Nuclear results from the implosion with the largest drive asymmetry are shown in Figure 2. Locations are given in spherical coordinates, with $\theta = 0°$ (vertical) aligned with Fig. 1(a)'s hohlraum axis and ϕ around the hohlraum's azimuth. Neutron time-of-flight diagnostics (nToF) [22] at four locations measure the neutron spectrum along a line-of-sight (LoS) by determining its arrival time from the effectively instantaneous emission (~0.1 ns). By taking moments of this spectrum with respect to time, we derived the neutron yield [23], bulk hot-spot velocity [24] and apparent ion temperature, T_{ion} [25,26,27]. Measured values for these quantities are shown next to each LoS. These four LoS velocities were used to solve for three hot spot velocity components (v_x, v_y, v_z) plus an isotropic component due to the reactants' thermal energy. The resulting hot-spot drift
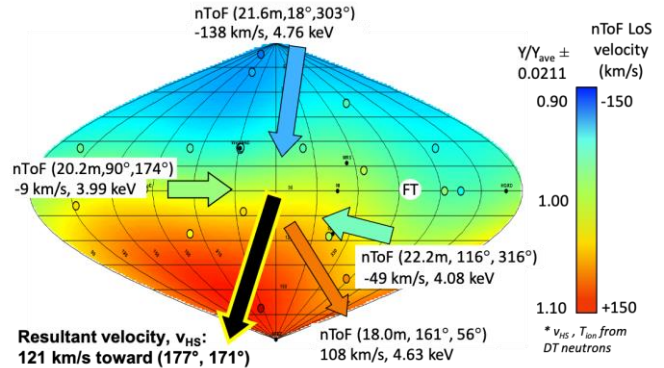
velocity for this case corresponds to a magnitude and direction of 121 ± 15 km/s toward (177°, 171°).

Independent confirmation of this velocity is provided by flange neutron activation detectors (FNADs), comprising 24 zirconium samples distributed around the target chamber [28]. Since $^{90}Zr(n, 2n)^{89}Zr$ activation cross-section increases with energy [29,30], any energy increase given to the 14.028-MeV DT neutrons from the reactants' center-of-mass velocity will produce higher activation in the direction of that velocity. A spherical-harmonic expansion has been fit to the activation data from each Zr detector, and is shown in Figure 2 as an underlaid colormap. The peak activation (red) tightly correlates with the resultant v_{HS} derived from nToF measurements. Furthermore, this activation difference arises from velocity effects and not from areal density [31], as expected for this gas-filled implosion with fuel and shell areal densities of only ~0.1 g/cm^2 and 0.4 g/cm^2, respectively. These independent measures of v_{HS} were consistent across all implosions in this series. The agreement across multiple, independent diagnostics provides confidence that observed velocities are indeed produced by the imposed laser asymmetry.

Drive-asymmetry signatures in x-ray [32,33] and neutron imaging [34,35,36] are shown in Figure 3. Time-integrated $\lesssim 8$ keV x-ray imaging is presented along two sightlines: top row looking from (090°, 100°) and bottom row from (090°, 315°). The imposed drive asymmetries vary from $-P1/P0$ to nominally balanced to $+P1/P0$. v_{HS} vectors (white arrows) are projected into each image's LoS. Here $P1/P0$ is defined as the Legendre decomposition of drive into its first mode $P1$, and normalized to the 0th mode $P0$ [37].

The top row of Figure 3 shows this velocity correlates with shell limb brightening in all cases, which is indicative of hot fuel depositing energy in the remaining HDC [38]. The bottom row of Figure 3 overlays neutron
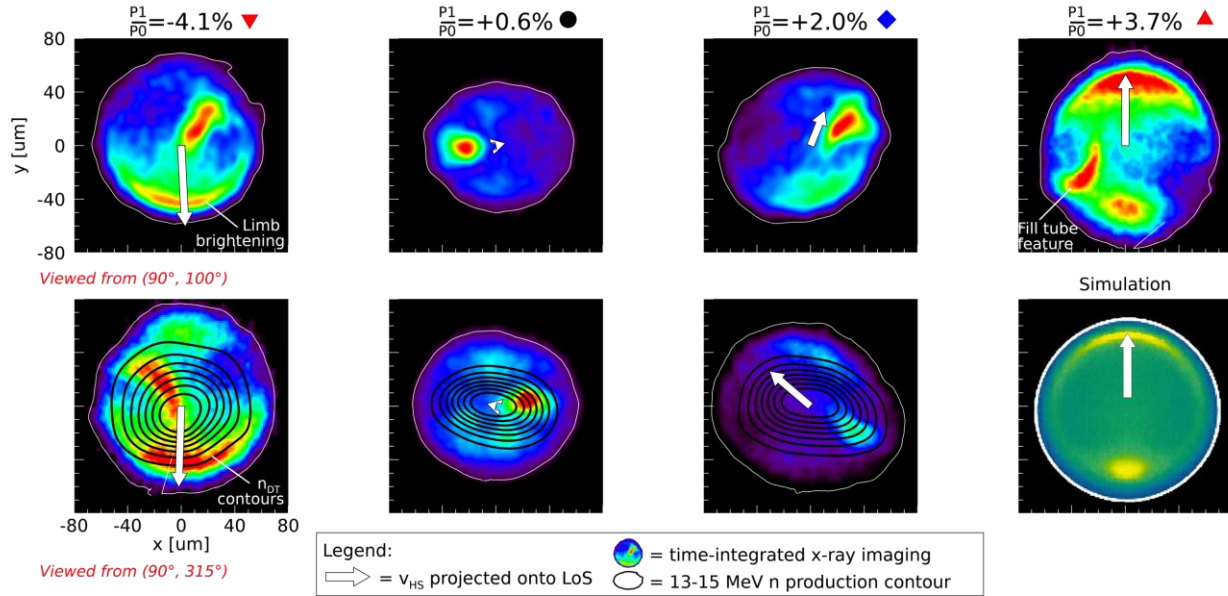
Figure 3: nToF bulk velocities (white arrows) are consistent with features inside the hot spot.
Top row: x-ray limb brightening and fill tube streak are correlated with v_{HS}. Bottom row: overlaid 13-15 MeV n production contours, evenly spaced from 17% - 95%. From left to right, v_{HS}: (121±15 km/s, 177±14°, 171±168°); (78±20 km/s, 24±22°, 243±43°); (15±22 km/s, 95±70°, 155±89°); (118±16 km/s, 8±12°, 356±95°).

production contours onto co-located x-ray images. Note the "streak" present in all images is due to high-Z dopant entrained by a fill-tube induced jet, as will be discussed below, and was not included in the 2D simulations presented herein.

The far-right column in Figure 3 compares measured x-ray imaging with a synthetic x-ray image from 2D HYDRA modeling [39], both with similar drive asymmetry. In both images two distinct features are observed: increased x-ray emission in the direction of v_{HS} (white arrow) and also diametrically opposite. Note the fill tube was not included in these simulations. X-ray emission is proportional to n and T, and simulations have suggested fluid motion within the hot spot can lead to increased temperature parallel to v_{HS} and increased density anti-parallel to v_{HS} [see ref. 5, Fig. 3]. New simulations, shown below and in the Supplementary Material, suggest fuel at the north pole is pushed out of the way of this incoming jet, travels around the hot spot periphery confined by the imploding shell, and stagnates near the south pole. This increased density leads to increased x-ray emission. While not conclusive, observed x-ray images are strikingly similar to those generated by vortical flows in simulations.

Global, burn-averaged quantities also trend similarly between simulation and observation as shown in Figure 4. A series of 2D HYDRA capsule-only simulations imposed increasing $P1/P0$ drive-asymmetries and tallied quantities using synthetic diagnostics along representative lines-of-sight. Simulation outputs (empty symbols) and experimental measurements (stars) are compared versus $P1/P0$ drive asymmetry.

Experimental $P1/P0$ values are estimated from viewfactor calculations using asymmetries in measured laser delivery and hohlraum structure, including diagnostic windows [40]. Fits to the data are described in the Supplementary Material. Simulated $P1/P0$ values trend with observations though lie outside experimental uncertainties. As seen, the $P1/P0$ value derived for N171112 is anomalously low given its drift velocity. The batch of ablator capsules from which this shell originated is suspected to have mass differentials in the poles, which serves to increase the measured drift velocity for no increase in applied laser $P1$ [41, 42].

Experimentally measured yields decrease more rapidly than simulation [Figure 4(b)]. However, both fall
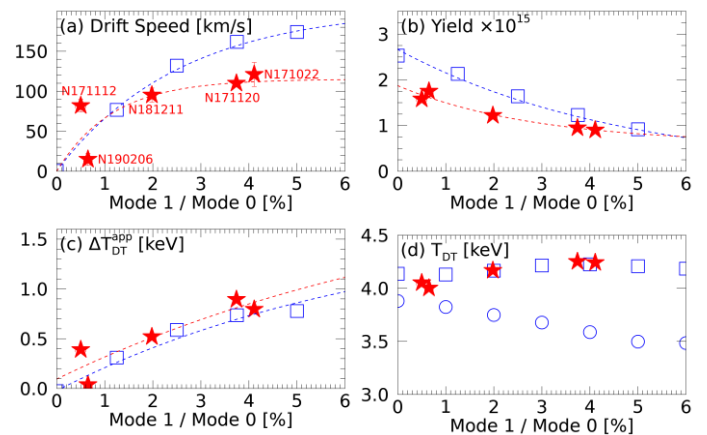
Figure 4: Measured (stars) and simulated (empty) values vs Mode 1/Mode 0 amplitude for (a) v_{HS}, (b) DT-neutron yield, (c) T_{DT}^{app} anisotropy, and (d) T_{DT}^{app} and $T_{DT, thermal}$ (circles).
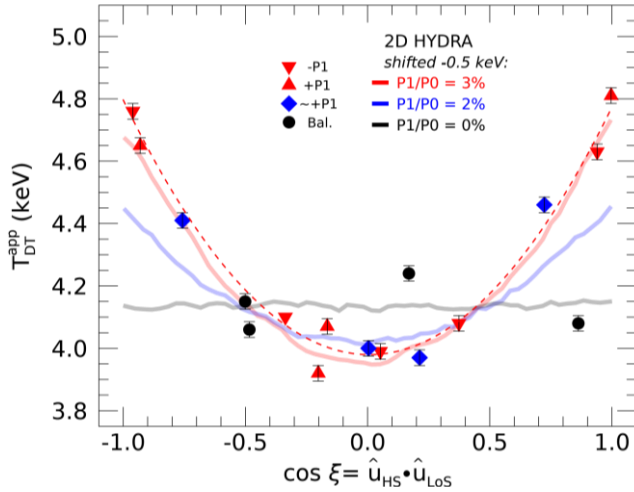
Figure 5: Apparent T_{ion} vs angle between observer and v_{HS}. Symbols are measured values and suggest applied asymmetry (i.e. ▼ for -P1). Solid lines are simulations uniformly shifted by -0.5 keV. Dashed red line is theoretical calculation from Eq. (1).

more slowly than previous simulations of DT-layer, CH-capsules driven by a "low-foot" laser pulse [5], suggesting layered implosions are even more sensitive to $P1/P0$ asymmetries than gas-filled capsules used here.

It has been established that apparent T_{DT} derived from nToF measurements is increased by the variance in the reacting fuel's velocity distribution [3,16,43]. nToF views parallel to the induced v_{HS} often see increased velocity-variance and hence broadened T_{DT}; herein we distinguish that observable as "apparent T_{DT}" (T_{DT}^{app}). Figure 4(c) plots the growth in the maximum apparent temperature *difference*, ΔT_{DT}^{app}, as observed along different nToF LoS. We find that as asymmetric drive increases, the contribution of flow variance to T_{DT}^{app} also increases. This trend is confirmed by experiment and simulation. In Figure 4(d) simulations show the actual thermal ion temperature decreases as implosions become increasingly perturbed; however, a simple average of the T_{DT}^{app} over 4π steradians remains almost constant since it is broadened by increased flow variance from the induced v_{HS}. This broadening roughly cancels the lost spectral-width as thermal T_{DT} decreases, and is consistent with the average T_{DT}^{app} from measured DT neutron spectra.

To exhibit this velocity variance effect on neutron spectral broadening, in Figure 5 we plot the measured T_{DT}^{app} values from four implosions with varied $P1/P0$ amplitudes versus the cosine of their observation angle, ξ. Here ξ is defined as the angle between the detector LoS and the v_{HS} direction. When $\cos\xi = +/-1$, the LoS and flow direction are parallel/antiparallel, respectively. Even though v_{HS} changes sign between parallel/antiparallel LoS (e.g. Figure 2), the velocity *variance* is positive definite and thus broadens the observed neutron spectrum

equally for angles $\pm\xi$ with respect to v_{HS}. This has been derived mathematically [27]:

$$Var(\omega) = \langle\tau\rangle + Var(u_{\parallel}) + \cdots \qquad (1)$$

where ω is the scaled, shifted neutron momentum [15], $Var(\omega) = \langle\omega^2\rangle - \langle\omega\rangle^2$ is the square of the standard deviation of the observed distribution, $\langle\tau\rangle$ is the mean, or apparent, temperature, and $Var(u_{\parallel})$ is the variance of the velocity parallel to the observer's line-of-sight. This theoretical relationship is plotted for the $\pm P1$ case in Fig. 5 (dashed red). From this formalism, measurements shown correspond to velocity variances of $(130$ km/s$)^2$, $(100$ km/s$)^2$, $(0$ km/s$)^2$ for decreasing $P1/P0$ magnitudes.

The results from 2D HYDRA simulations are overlaid in the figure as solid lines. Note 2D HYDRA overpredicts the absolute ion temperature by roughly 0.5 keV though exhibits identical trends as the measurements. Also in both simulation and data the minimum T_{DT}^{app} decreases with increasing $P1/P0$ magnitude, which implies the implosion becomes increasingly perturbed and loses more energy to residual kinetic energy.

Figure 5 shows consistency between measurement, simulation, and theory for the effects of a $P1/P0$ perturbation on T_{DT}^{app}. As $P1/P0$ increases, all three agree that flow variance increases the T_{DT}^{app} due to reactants' initial velocities. A direct measurement of the expected flow-variance broadening could be obtained by mapping out reactant velocity streamlines.

We accomplish this by the method shown in Figure 6(a), which shows a time-sequence of x-ray emission images measured perpendicular to the $-P1/P0$ direction [44,45,46]. A bright emission region originates at the angular location of the fill tube and traverses the hot spot over time. During an implosion the fill tube entrains a jet of material ahead of the main shock [47,48,49], which in these capsules includes a high-Z tungsten dopant. This entrained material emits x-rays more strongly than background deuterium or tritium and serves as a tracer particle for flows internal to the hot spot. It is observed in all drive cases in this study.

Figures 6(b,c) show results of tracking this tracer (centroid of 90% contour) through the hot spot over time [50]. Motion is decomposed into horizontal and vertical velocities and shown for three applied drives. Symbols correspond to the applied perturbation direction: $+P1/P0$ (Δ), balanced ($\circ$), and $-P1/P0$ (∇). Horizontal velocities [Fig. 6(b)] remain negative and approximately constant over time, indicative of radially-inward motion with little or no drive perturbation in the horizontal direction. This large horizontal velocity, aligned with initial fill tube axis and impervious to drive asymmetry, has been predicted by simulations [47,48] and is unrelated to imposed $P1/P0$.
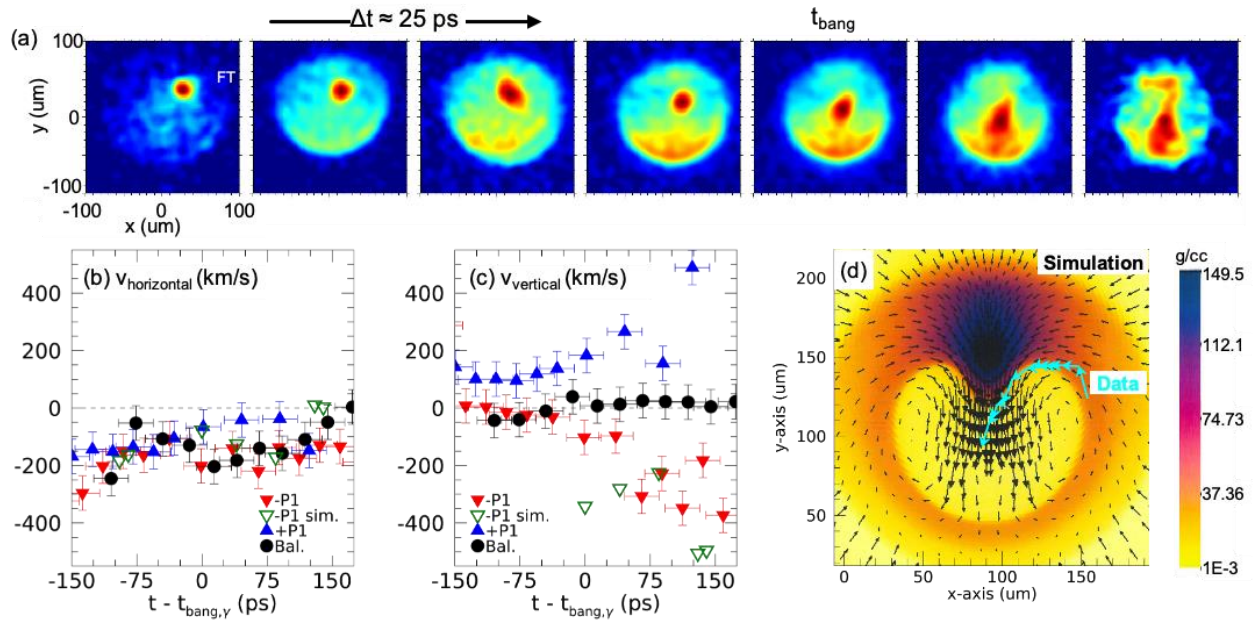
Figure 6: Measured and simulated flow within imploding ICF hot spots. (a) Time-resolved sequence of measured x-ray emission during a single implosion, viewed orthogonal to imposed asymmetry. (b) Horizontal and (c) vertical flow velocity for three asymmetry drives. (d) Streamline data of internal flows from -P1/P0, overlaid on flow field from 2D HYDRA simulation at t_{bang} + 65 ps.

Simulated values at similar times and locations to measurements (hollow triangles) lie within uncertainties.

  In contrast, vertical acceleration is clearly observed in imbalanced cases and is correlated with the drive asymmetry direction [Fig 6(c)]. Observed vertical flow velocities exceed 250 km/s at late times in the most imbalanced cases. Prediction from simulations (hollow green triangles) support internal flows of these magnitudes and directions. This is the first direct observation of hydrodynamic fuel flow during imploding ICF plasmas, with densities and pressures exceeding 10 g/cm³ and 10 Gbar, respectively. Maximum, instantaneous velocities are larger than nToF bulk flows (Fig. 3) since measured-v_{HS} is necessarily temporally- and spatially-averaged. As the implosion evolves through peak fusion yield ($t = t_{bang,\gamma}$) the measured v_{HS} is a convolution of the instantaneous velocity field with the neutron production field, at each instant in time. Assuming a Gaussian burn profile of measured duration [51], the convolution for the $-P1/P0$, $+P1/P0$, and balanced implosions shown are -113 km/s, 153 km/s, and 3 km/s, respectively. Note the $+P1/P0$ case is heavily influenced by the >400 km/s measurement, and excluding that point returns 129 km/s. These burn-averaged velocities are consistent and within uncertainties of measured nToF v_{HS} above.

  An additional consideration lies in flows that counter-propagate around the hot spot periphery as described above. This motion sets up a vortical flow pattern suggested by previous simulations [4, 52] and shown here from 2D HYDRA calculations of these implosions [Fig. 6(d), and Supplementary Material]. The *measured* path during one implosion is overlaid on simulated velocity (arrows) and density (colormap) fields. Each point in this path is determined by the tracer's centroid at a given time, and the velocity vector is drawn based on v_{horiz} and v_{vert} at that time. The simulation shown is at $t_{bang} + 65\ ps$, though similar flow behavior is seen throughout. Near the bottom of the shell the velocity is seen to turn up and outward, implying counter-propagating flows along the hot spot edge. When observed along a single nToF LoS this retrograde motion necessarily contributes to velocity-variance and hence broadens T_{DT}^{app}. Lines-of-sight parallel to the simulated-$P1/P0$ will see increased variance while those normal will not, which is consistent with measured T_{DT}^{app} values in Figure 5.

  In summary, deleterious effects of asymmetric drive on implosion performance have been quantified. The broadened neutron energy spectra are in agreement with expectation from simulated bidirectional motion of these flows. Time-resolved flows internal to the hot spot are visualized for the first time using a natural tracer jet. Simulations trend similarly to measurements as a function of hot-spot velocity. This work identifies and quantifies a major degradation source relevant for ignition-type targets.

Livermore National Security, LLC, nor any of their employees makes any warranty, expressed or implied, or assumes any legal liability or responsibility for the accuracy, completeness, or usefulness of any information, apparatus, product, or process disclosed, or represents that its use would not infringe privately owned rights. Reference herein to any specific commercial product, process, or service by trade name, trademark, manufacturer, or otherwise does not necessarily constitute or imply its endorsement, recommendation, or favoring by the United States government or Lawrence Livermore National Security, LLC. The views and opinions of authors expressed herein do not necessarily state or reflect those of the United States government or Lawrence Livermore National Security, LLC, and shall not be used for advertising or product endorsement purposes. LLNL-JRNL-776860-DRAFT

[1] O.A. Hurricane, D.A. Callahan, D.T. Casey, P.M. Celliers, C. Cerjan, E.L. Dewald, *et al.*, Nature **506**, 343 (2014).

[2] C.K. Li, F.H. Séguin, J.A. Frenje, R.D. Petrasso, J.A. Delettrez, P.W. McKenty, *et al.*, Phys. Rev. Lett. **92**, 205001, 2004.

[3] M. Gatu Johnson, J.P. Knauer, C.J. Cerjan, M.J. Eckart, G.P. Grim, E.P. Hartouni, *et al.*, Phys. Rev. E **94**, 021202(R) (2016).

[4] M. Gatu Johnson, B.D. Appelbe, J.P. Chittenden, J. Delettrez, C. Forrest, J.A. Frenje, *et al.*, Phys. Rev. E **98**, 051201(R) (2018).

[5] B.K. Spears, M.J. Edwards, S. Hatchett, J. Kilkenny, J. Knauer, A. Kritcher, *et al.*, Phys. Plasmas **21**, 042702 (2014).

[6] G.A. Kyrala, J.L. Kline, S. Dixit, S. Glenzer, D. Kalantar, D. Bradley, *et al.*, Phys. Plasmas **18**, 056307 (2011).

[7] D. Eder, B. Spears, D. Casey, A. Pak, T. Ma, N. Izumi, *et al.*, Journal of Physics: Conference Series **717**, 012014 (2016).

[8] M. Gatu Johnson, D.T. Casey, J.A. Frenje, C.-K. Li, F.H. Séguin, R.D. Petrasso, *et al.*, Phys. Plasmas 20, 042707 (2013).

[9] C.R. Christensen, D.C. Wilson, C.W. Barnes, G.P. Grim, G.L. Morgan, M.D. Wilke, F.J. Marshall, V.Yu. Glebov, and C. Stoeckl, Phys. Plasmas **11**, 2771 (2004).

[10] A. Pak, L. Divol, C.R. Weber, L.F. Berzak Hopkins, D.S. Clark, E.L. Dewald, *et al.* Phys. Rev. Lett. **124**, 145001 (2020).

[11] L.A. Pickworth, B.A. Hammel, V.A. Smalyuk, H.F. Robey, R. Tommasini, L.R. Benedetti, *et. al.,* Phys. Plasmas **25**, 082705 (2018).

[12] D.T. Casey, B.J. MacGowan, J.D. Sater, A.B. Zylstra, O.L. Landen, J. Milovich, *et al.,* Phys. Rev. Lett. **126**, 025002 (2021).

[13] O.L. Landen, D.T. Casey, J-M DiNicola, T. Doeppner, E.P. Hartouni, D.E. Hinkel, *et al.*, High Energy Density Physics **36**, 100755 (2020).

[14] D.S. Clark, C.R. Weber, A.L. Kritcher, J.L. Milovich, P.K. Patel, S.W. Haan, *et al.*, Phys. Plasmas **26**, 050601 (2019).

[15] D.H. Munro, J.E. Field, R. Hatarik, J.L. Peterson, E.P. Hartouni, B.K. Spears, and J.D. Kilkenny, Phys. Plasmas **24**, 056301 (2017).

[16] B. Appelbe and J. Chittenden, Plasma Phys. Control. Fusion **53** 045002 (2011).

[17] T.J. Murphy, Phys. Plasmas **21**, 072701 (2014).

[18] L. Berzak Hopkins, L. Divol, C. Weber, S. Le Pape, N.B. Meezan, J.S. Ross, *et al.*, Phys. Plasmas **25**, 080706 (2018).

[19] D.D.-M. Ho, S.W. Haan, J.D. Salmonson, D.S. Clark, J.D. Lindl, J.L. Milovich, C.A. Thomas, L.F. Berzak Hopkins and N.B. Meezan, Journal of Phys. **717**, 012023 (2016).

[20] K.L. Baker, C.A. Thomas, D.T. Casey, S. Khan, B.K. Spears, R. Nora, *et al.*, Phys. Rev. Lett. **121**, 135001 (2018).

[21] D.T. Casey, C.A. Thomas, K.L. Baker, B.K. Spears, M. Hohenberger, S.F. Khan, *et al.*, Phys. Plasmas **25**, 056308 (2018).

[22] V. Yu. Glebov, T.C. Sangster, C. Stoeckl, J.P. Knauer, W. Theobald, K.L. Marshall, *et al.*, Rev. Sci. Instrum. **81**, 10D325 (2010).

[23] R. Hatarik, D.B. Sayre, J.A. Caggiano, T. Phillips, M.J. Eckart, E.J. Bond, *et al.*, Journal Applied Phys. **118**, 184502 (2015).

[24] R. Hatarik, R.C. Nora, B.K. Spears, M.J. Eckart, G.P. Grim, E.P. Hartouni, A.S. Moore, and D.J. Schlossberg, Rev. Sci. Instrum. **89**, 10I138 (2018).

[25] H. Brysk, Plasma Phys. **15**, 611 (1973).

[26] B. Appelbe, and J. Chittenden, High Energy Density Physics **11**, 30 (2014).

[27] D.H. Munro, Nucl. Fusion **56**, 036001 (2016).

[28] C.B. Yeamans and D.L. Bleuel, Fusion Sci. and Tech. **72**, 120 (2017).

[29] A. Pavlik, G. Winkler, H. Vonach, A. Paulsen, and H. Liskien, J. Phys. G: Nucl. Phys. **8**, 1283 (1982).

[30] J.D. Kilkenny, J.A. Caggiano, R. Hatarik, J.P. Knauer, D.B. Sayre, B.K. Spears, *et al.*, Journal of Physics **688**, 012048 (2016).

[31] H.G. Rinderknecht, R. Bionta, G. Grim, R. Hatarik, H. Khater, D. Schlossberg, and C. Yeamans, Rev. Sci. Instrum. **89**, 10I125 (2018).

[32] P.M. Bell, D.K. Bradley, J.D. Kilkenny, A. Conder, C. Cerjan, C. Hagmann, *et al.*, Rev. Sci. Instrum. **81**, 10E540 (2010).

[33] L.R. Benedetti, P.M. Bell, D.K. Bradley, C.G. Brown, S.M. Glenn, R. Heeter, *et al.*, Rev. Sci. Instrum. **83**, 10E135 (2012).

[34] D.B. Ress, R.A. Lerche, R.J. Ellis, S.M. Lane, and K.A. Nugent, Science **241**, 956 (1988).

[35] G.P. Grim, C.W. Barnes, P.A. Bradley, C.R. Christensen, A. Hauer, G.L. Morgan, *et al.*, J. Phys. IV France **133**, 913 (2006).

[36] P. Volegov, C.R. Danly, D.N. Fittinghoff, G.P. Grim, N. Guler, N. Izumi, *et al.*, Rev. Sci. Instrum. **85**, 023508 (2014).

[37] C.V. Young, L. Masse, D.T. Casey, B.J. MacGowan, O.L. Landen, D.A. Callahan, *et al.*, Phys. Plasmas **27**, 082702 (2020).

[38] L.A. Pickworth, B.A. Hammel, V.A. Smalyuk, H.F. Robey, L.R. Benedetti, L. Berzak Hopkins, *et al.*, Phys. Plasmas **25**, 054502 (2018).

[39] M.M. Marinak, G.D. Kerbel, N.A. Gentile, O. Jones, D. Munro, S. Pollaine, T.R. Dittrich, and S.W. Haan, Phys. Plasmas **8**, 2275 (2001).

[40] B.J. MacGowan, O.L. Landen, D.T. Casey, C. Young, D.A. Callahan, E.P. Hartouni, *et al.*, High Energy Density Physics, accepted (2021).

[41] O.A. Hurricane, D.T. Casey, O. Landen, A.L. Kritcher, R. Nora, P.K. Patel, *et al.*, Phys. Plasmas **27**, 062704 (2020).

[42] D.T. Casey, O.L. Landen, E. Hartouni, R.M. Bionta, K.D. Hahn, P.L. Volegov, *et al.*, Phys. Plasmas **28**, 042708 (2021).

[43] L.C. Jarrott, B. Bachmann, T. Ma, L.R. Benedetti, J.E. Field, E.P. Hartouni, *et al.*, Phys. Rev. Lett. **121**, 085001 (2018).

[44] J.D. Kilkenny, P. Bell, R. Hanks, G. Power, R.E. Turner, and J. Wiedwald, Rev. Sci. Instrum. (invited) **59**, 1793 (1988).

[45] S.M. Glenn, L.R. Benedetti, D.K. Bradley, B.A. Hammel, N. Izumi, S.F. Khan, *et al.* Rev. Sci. Instrum. **83**, 10E519 (2012).

[46] S.F. Khan, N. Izumi, S. Glenn, R. Tommasini, L.R. Benedetti, T. Ma, *et al.* Rev. Sci. Instrum. **87**, 11E334 (2016).

[47] T.R. Dittrich, O.A. Hurricane, L.F. Berzak-Hopkins, D.A. Callahan, D.T. Casey, D. Clark, *et al.*, Journal of Physics: Conference Series **717**, 012013 (2016).

[48] C.R. Weber, D.S. Clark, A. Pak, N. Alfonso, B. Bachmann, L.F. Berzak Hopkins, *et al.*, Physics of Plasmas **27**, 032703 (2020).

[49] K.L. Baker, C.A. Thomas, T.R. Dittrich, O. Landen, G. Kyrala, D.T. Casey, *et al.*, Physics of Plasma **27**, 112706 (2020).

[50] J.J. Ruby, A. Pak, J.E. Field, T. Ma, B.K. Spears, L.R. Benedetti, *et al.*, Physics of Plasmas **23**, 072701 (2016).

[51] H.W. Herrmann, N. Hoffman, D.C. Wilson, W. Stoeffl, L. Dauffy, Y.H. Kim, *et al.*, Rev. Sci. Instrum. **81**, 10D333 (2010).

[52] V.A. Thomas and R.J. Kares, Phys. Rev. Lett. **109**, 075004 (2012).